Biogeochemistry
DOI 10.1007/s10533-015-0165-5

Geochemical drivers of organic matter decomposition in arctic tundra soils

Elizabeth M. Herndon · Ziming Yang · John Bargar · Noemie Janot · Tom Z. Regier · David E. Graham · Stan D. Wullschleger · Baohua Gu · Liyuan Liang

Received: 8 April 2015 / Accepted: 16 November 2015

Abstract Climate change is warming tundra ecosystems in the Arctic, resulting in the decomposition of previously-frozen soil organic matter (SOM) and release of carbon (C) to the atmosphere; however, the processes that control SOM decomposition and C emissions remain highly uncertain. In this study, we evaluate geochemical factors that influence microbial production of carbon dioxide (CO_2) and methane (CH_4) in the seasonally-thawed active layer of interstitial polygonal tundra near Barrow, Alaska. We report spatial and seasonal patterns of dissolved gases in relation to the geochemical properties of Fe and organic C in soil and soil solution, as determined using spectroscopic and chromatographic techniques. The chemical composition of soil water collected during the annual thaw season varied significantly with depth. Soil water in the middle of the active layer contained abundant Fe(III), and aromatic-C and low-molecular-weight organic acids derived from SOM decomposition. At these depths, CH_4 was positively correlated with the ratio of Fe(III) to total Fe in waterlogged transitional and low-centered polygons but negatively correlated in the drier flat- and high-centered polygons. These observations contradict the expectation

Responsible Editor: Stephen Porder.

Electronic supplementary material The online version of this article (doi:10.1007/s10533-015-0165-5) contains supplementary material, which is available to authorized users.

E. M. Herndon · Z. Yang · S. D. Wullschleger · B. Gu · L. Liang (✉)
Environmental Sciences Division, Oak Ridge National Laboratory, P.O. Box 2008, MS-6036, Oak Ridge, TN 37831, USA
e-mail: liangl@ornl.gov

J. Bargar · N. Janot
Stanford Synchrotron Radiation Lightsource, SLAC National Accelerator Laboratory, Menlo Park, CA 94025, USA

T. Z. Regier
Canadian Light Source, Saskatoon, SK S7N 2 V3, Canada

D. E. Graham
Biosciences Division, Oak Ridge National Laboratory, Oak Ridge, TN 37831, USA

Present Address:
E. M. Herndon (✉)
Department of Geology, Kent State University, Kent, OH 44242, USA
e-mail: eherndo1@kent.edu

N. Janot
Laboratoire Interdisciplinaire des Environnements Continentaux (LIEC), UMR 7360 CNRS-Université de Lorraine, 15 Avenue du Charmois, 54500 Vandoeuvre, France

Published online: 07 December 2015

that CH_4 would be uniformly low where Fe(III) was high due to inhibition of methanogenesis by Fe(III)-reduction reactions. Our results suggest that vertically-stratified Fe redox reactions influence respiration/fermentation of SOM and production of substrates (e.g., low-molecular-weight organic acids) for methanogenesis, but that these effects vary with soil moisture. We infer that geochemical differences induced by water saturation dictate microbial products of SOM decomposition, and Fe geochemistry is an important factor regulating methanogenesis in anoxic tundra soils.

Keywords Iron biogeochemistry · Tundra soil · Active layer · Soil organic matter · Methane

Introduction

Arctic tundra soils store large quantities of organic carbon that could be readily decomposed and released as carbon dioxide (CO_2) and methane (CH_4) as global temperatures rise (Heimann and Reichstein 2008; Tarnocai et al. 2009; Stocker et al. 2013). Tundra ecosystems may serve as a net sink or source of carbon under a warmer climate depending on the balance between C-fixation by plants (sink) and C-release by microbial decomposition (source) (e.g., Schuur et al. 2009; Sturtevant and Oechel 2013; Ueyama et al. 2013). Decomposition is currently limited by sub-freezing temperatures, resulting in slow rates of microbial metabolism and limited access to unfrozen carbon substrates. Continued warming will increase microbial activity and thaw depth, enhancing the breakdown of soil organic matter (SOM) to form CO_2 and CH_4 (Schuur et al. 2008; Schuur et al. 2009; Koven et al. 2015). In order to predict how C budgets in tundra soils will respond to increased temperature, it is necessary to understand the coupled chemical and microbial processes that release or retain C in the deepening tundra thaw layer.

In low-relief tundra ecosystems, the quantities and relative proportions of CO_2 and CH_4 produced by microorganisms depend on conditions of water-saturation that are controlled by microtopographic features of the landscape (Lipson et al. 2010; Zona et al. 2012). At relatively high topographic positions, soils are well-drained and aerobic respiration facilitates decomposition of SOM to release stored C primarily as CO_2 (e.g. Zona et al. 2011). In low-lying soils where water-saturation limits oxygen diffusion, anaerobic metabolisms (e.g., fermentation, Fe-reduction, and methanogenesis) release both CO_2 and CH_4 (Turetsky et al. 2008; Zona et al. 2012; Sturtevant and Oechel 2013). Although widespread soil drying is predicted for high-latitude ecosystems (Smith et al. 2005; Hinzman et al. 2013), it is anticipated that CH_4 emissions from tundra will increase by the end of the century due rising temperatures in areas that remain inundated (Zhuang et al. 2007; Turetsky et al. 2008; Stocker et al. 2013; Kim 2015). However, the biogeochemical reactions that govern the evolution of greenhouse gases in anoxic tundra soils represent a major uncertainty in global climate models (Riley et al. 2011).

Geochemical factors (e.g., pH, soil mineralogy, electron acceptor availability) strongly influence CO_2 and CH_4 production in anoxic, water-saturated soils. In particular, interactions between iron, organic C, and microorganisms potentially control SOM decomposition and greenhouse gas production. Iron in the form of oxyhydroxide minerals (e.g., ferrihydrite) chemically binds and physically protects C substrates, limiting their bioavailability until SOM desorption or Fe reduction occurs (Gu et al. 1994, 1995; Baldock and Skjemstad 2000; Liang et al. 2000). Additionally, Fe(III) can serve as terminal electron acceptor for microbial respiration of organic matter. Lipson et al. (2010, 2012, 2013) report that iron (Fe) reduction dominates anaerobic respiration in shallow peat soils located on the Arctic coastal plain near Barrow, Alaska. These saturated, organic-rich soils contain high concentrations of dissolved and colloidal Fe that undergo seasonal redox cycling due to microbial activity and fluctuations in the water table. In such systems where Fe(III) is abundant, methane production is typically suppressed because Fe-reducing microorganisms that produce CO_2 outcompete methanogens for C substrates (Roden and Wetzel 1996; Metje and Frenzel 2007; Lipson et al. 2012). Although Fe cycling can impact the decomposition of soil organic matter through both physical and chemical processes, the specific interactions and reaction pathways are not well understood for Arctic ecosystems.

The present study was undertaken to evaluate biogeochemical processes that facilitate anaerobic production of CO_2 and CH_4 in tundra soils at the Barrow Environmental Observatory (BEO). Our

investigation targeted four ice-wedge polygons that represent dominant geomorphic features on the landscape and span a hydrological gradient from poorly-drained to well-drained soils (Hubbard et al. 2013). Our study focused on vertical gradients of aqueous geochemistry in the active layer, i.e. the seasonally-thawed upper soil layer that overlies permafrost. In particular, we examined spatial and seasonal patterns of dissolved CO_2 and CH_4 in relation to the geochemical properties of iron and organic matter in order to elucidate pathways of SOM decomposition. We hypothesized that aqueous geochemistry and CO_2 and CH_4 concentrations would vary with depth in the active layer due to differences in soil saturation and microbial decomposition pathways. We predicted that (i) abundant Fe(III) near the soil surface would facilitate anaerobic oxidation of organic matter, and (ii) dissolved CH_4 concentrations would be low in areas where Fe(III) concentrations were high given that iron-reducing microorganisms outcompete methanogens for organic substrates. Using chromatographic and spectroscopic techniques, we identified dissolved Fe species and low-molecular-weight organic acids and examined the effect of iron cycling on SOM decomposition and CO_2 and CH_4 concentrations. We propose that climate driven changes in water saturation, which in turn alters chemical gradients, may profoundly influence the microbial degradation of SOM and greenhouse gas production in the warming Arctic tundra.

Methods

Field measurements and sampling

This field study was conducted at the BEO located in the Arctic coastal plain region of northern Alaska in the United States. Although mean annual precipitation in the region is low (12 cm $year^{-1}$ rainfall + 75 cm $year^{-1}$ snowfall; WRRC 1949–2005), the landscape is largely water saturated due to poor drainage from underlying permafrost (Bockheim et al. 1999). Topographic relief along the coastal plain is minimal and contributes to a landscape that is dominated by small lakes, drained thaw lake basins, and interstitial polygonal terrain (Brown et al. 1980; Hinkel et al. 2005). Polygons consist of microtopographic features (polygon centers, troughs, and ridges—e.g., Fig. 1) that alter water flow and generate sharp redox gradients across centimeter-scale depths (Zona et al. 2011).

Geochemistry was examined across four types of polygons that span a development sequence from waterlogged drained thaw-lake soils to well-drained and "degraded" polygonal ground at the BEO (Fig. 1 and S1): a transitional polygon (i.e., transitional between the drained thaw-lake basins and a low-centered polygon), a low-centered polygon (LCP), a flat-centered polygon (FCP, transitional from low to high-centered polygons), and a high-centered polygon (HCP). These polygons were selected as intensive study sites for the Next Generation Ecosystem Experiments because they represent dominant landscape geomorphology (Hubbard et al. 2013) and can be used to build a predictive scaling framework for climate models. Moisture regimes in these soils range from wet and moist-wet (transitional and LCP) to moist-dry and dry (FCP and HCP) (Lara et al. 2014). Active layer thickness was measured at each sampling location by inserting a pointed metal probe vertically into the ground to the depth of resistance, i.e., the thaw depth. Volumetric soil moisture (m^3/m^3) was recorded in unsaturated surface soils (<10 cm) in early July using a 5TE soil moisture probe (decagon devices) calibrated to peat soils in the laboratory (Fig. 1). Shallow ground temperatures (<1.2 m depth) in the region are reported to range from less than −22 °C in the winter to approximately 4 °C in the summer, and temperature fluctuations are more pronounced near the soil surface than at depth (Hinkel et al. 2001; Shiklomanov et al. 2010).

Surface and soil water samples were collected in early July and late August in 2013 and 2014. Samples were obtained from all topographic positions that were present in a given polygon, i.e., the ridge and center in the transitional polygon, the trough, ridge, and center of the LCP and FCP, and the trough and center of the HCP (Fig. 1 and S1). Water samples were binned by sampling depths that correspond to surface water (0 cm), shallow soil water contained in the organic horizon (0–7 cm), intermediate soil water from the boundary between organic and mineral horizons (18–35 cm), and deep soil water from the mineral horizon (>35 cm). All depths are reported from the surface of the soil/moss layer (excluding overlying surface water) to the maximum sampling depth. Horizon boundaries were determined for soil cores collected from the LCP and HCP (Fig. S2) (Roy Chowdhury et al. 2015).

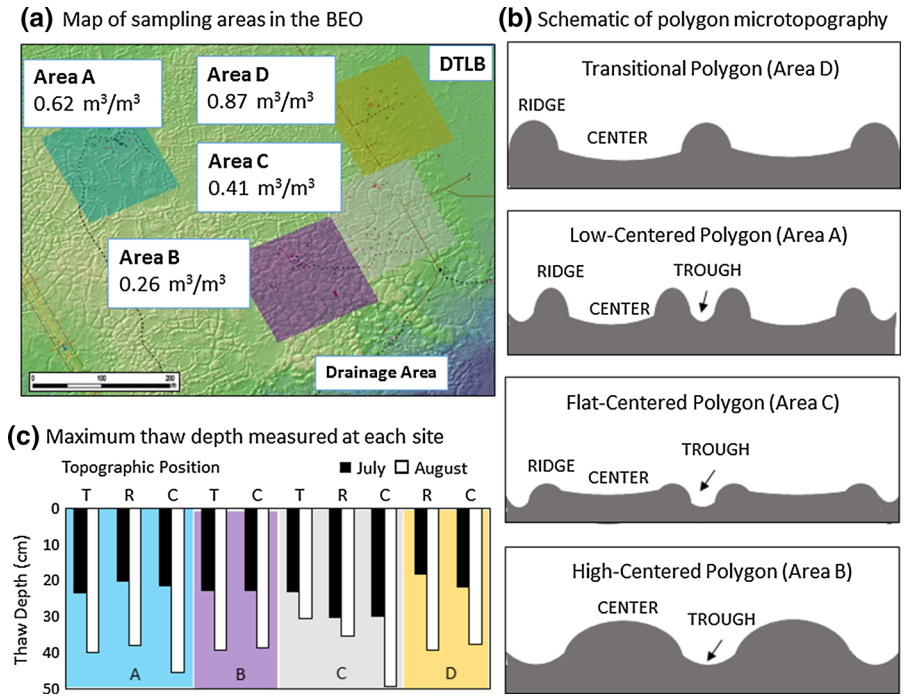

Fig. 1 **a** *Colored boxes* on the relief map of the Barrow Environmental Observatory indicate field sampling areas. Values for volumetric soil moisture (m^3/m^3) were measured in surface soils (<10 cm) at each site in early July. LiDAR image in Fig. 1a provided courtesy of Garrett Altmann (Los Alamos National Laboratory) and Craig Tweedie (University of Texas El Paso). **b** Diagrams of the different polygon types sampled in this study. Each *box* contains a cartoon of a polygon in cross-section view to highlight the relative elevations of the microtopographic features (ridge, center, trough) present in each polygon type. Elevation differences are not to scale. **c** The graph indicates maximum thaw depth measured at each topographic position (indicated by a T, C, or R) at each sampling site in early July (*black bar*) and late August (*white bar*)

Surface water was collected from areas where the water table was above the land surface. Macro rhizon samplers (Eijkelkamp), consisting of 9-cm long porous tubes with a nominal pore size of 0.1 μm, were used to collect pore waters from unsaturated shallow soils with 30-mL syringes under vacuum. The macrorhizons were inserted at a 45 degree angle to the soil surface to a maximum depth of 7 cm. Water that collected in the syringes overnight (<30 ml) was stored in acid-washed plastic vials for metal ion analysis and amber glass vials (combusted at 550 °C for 4 h) for dissolved organic carbon (DOC) analysis. Intermediate and deep soil waters were sampled from piezometers installed in the active layer of saturated soils. Piezometers, constructed from PVC pipes and slotted over the bottom 12 cm, were installed by hand-driving them to thaw depth in July and August. Additional piezometers were also installed to reach to the middle of the active layer in August. Note that thaw depth increased from July to August, and that thaw depth in early July was approximately equal to the middle of the active layer in August.

Water was collected by pulling through a 3.2-mm Teflon tubing into a 60 ml plastic syringe. Syringes and attached tubing were rinsed by collecting and discarding ~5 ml of sample water prior to the collection of each sample. Unfiltered surface and piezometer water were immediately transferred into combusted glass serum bottles with no headspace for pH, dissolved inorganic carbon, and dissolved CO_2 and CH_4 analyses in the laboratory. Sample bottles were crimp-capped with thick rubber stoppers. Additional bulk samples were collected in plastic bottles and subsequently vacuum-filtered (0.7 μm glass fiber +0.45 μm Supor filter) in the laboratory on the day of collection and stored in either acid-washed plastic bottles for cation and anion analysis or combusted glass vials for DOC analysis. Filtered samples were not acidified during storage due to a high concentration of humic acids which precipitate upon

acidification. All samples were transported to Oak Ridge National Laboratory in a cooler and stored at 4 °C prior to analyses.

Chemical analyses

Concentrations of dissolved ferrous iron (Fe(II)) in water samples were determined in the field using 1,10-phenanthroline colorimetric assay (Hach FerroVer). A Hach DR/900 colorimeter was calibrated with a ferrous ammonium sulfate standard (up to 3 ppm Fe(II)) both in the laboratory and in the field. Samples were filtered through syringe filters (0.7 μm glass fiber +0.45 μm GHP) immediately after water collection and analyzed for Fe(II) concentrations. Total Fe concentrations in water were measured by inductively coupled plasma mass spectrometry (ICP-MS), and dissolved ferric iron (Fe(III)) was calculated by subtracting Fe(II) from the total Fe. For samples with low Fe concentrations where the measured Fe(II) ≥ total Fe, Fe(II) was used as the total Fe and Fe(III) = 0. Electrical conductivity was measured on unfiltered samples in the field. One soil water sample collected from the center of the flat-centered polygon was excluded from further analyses due to abnormally high electrical conductivity values (>2500 μS cm^{-1}) that may result from mixing with a deeper saline layer (Newman et al. 2015). Water from this location contained high Cl concentrations (>15 mmol L^{-1}) in both 2012 and 2013. Due to the instability of the pH probe at near freezing conditions in the field, pH values were measured on unfiltered water in the laboratory.

Ion chromatography (IC) on a Dionex AS15 analytical column and an AG15 guard column was used to determine concentrations of common inorganic anions, including Cl^-, SO_4^{2-}, NO_3^-, Br^-, and PO_4^{3-}, and low-molecular weight organic acids, including acetate, formate, propionate, butyrate, succinate, tartrate, oxalate, fumarate, oxoglutarate, and citrate, in <0.45 μm filtered samples. Samples for organic acid analysis were acidified with hydrochloric acid while samples for inorganic anion analysis were not acidified. A multi-step gradient of increasing NaOH from 10 up to 80 mmol L^{-1} was applied to the columns with a Dionex EG40 eluent generator to elute the organic acids. Calibration curves for the inorganic anions and organic acid anions were generated with standard compounds and used to calculate anion concentrations.

Metal ions (Na, Ca, Mg, K, Fe, Mn, Al, et al.) were measured by inductively coupled plasma mass spectrometry (ICP-MS) following acidification with nitric acid. Samples containing high DOC (with notable brown colors) were treated with hydrogen peroxide (30 % w/w) under UV irradiation to remove organics prior to ICP-MS analysis. Dissolved inorganic carbon in water samples was determined by filtering (0.45 μm) just prior to analysis on a Shimadzu TOC-5000 analyzer. DOC concentrations were determined by the same analyzer for filtered samples that were diluted and acidified with hydrochloric acid prior to analysis.

Dissolved concentrations of CO_2 and CH_4 were determined for unfiltered water samples stored at 4 °C for less than one week in inverted 50 ml glass serum bottles with no headspace. To collect gas samples, we used an Ar gas pressurized syringe to displace 5 ml of water and create headspace in the serum bottle, which was then shaken lightly for 5 min to allow gas to reach the headspace. Duplicate 1 ml headspace samples were collected using gas-tight glass syringes and analyzed with gas chromatography (e.g., Roy Chowdhury et al. 2015). The composition of gas in the headspace was used to calculate concentrations of dissolved CH_4 and CO_2 in water using Henry's law and correcting for the solubility of CO_2 in water.

Soil cores from the trough, ridge, and center positions of the LCP were collected frozen in April 2012. Each soil core was subsequently thawed under N_2 atmosphere and homogenized by soil horizon as described by Roy Chowdhury et al. (2015). Subsamples were collected from the homogenized organic and mineral horizons to determine total concentrations of major cations. These samples were ground to <150 μm particle size, ashed at 550 °C, then fused with lithium metaborate at 900 °C for 10 min and subsequently dissolved in nitric acid. These solutions were analyzed for major cations (Fe, Al, K, Na, Mg, Ca, Si, Mn, P, Ti) on inductively coupled plasma atomic emission spectroscopy (ICP-AES) at the Laboratory for Isotopes and Metals in the Environment at The Pennsylvania State University. The organic horizon at the center location of the LCP center was not analyzed due to insufficient material. Bulk soil material was also collected at 10 cm increments from soil cores from the trough and center positions of the HCP. These soil samples were dried, ground with a mortar and pestle in an anaerobic glove

box, and analyzed using carbon X-ray absorption fine structure spectroscopy (detailed below).

Spectroscopic characterization of carbon and iron

Dissolved organic matter (DOM) in surface and soil pore waters was further characterized using ultraviolet–visible (UV–vis), Fourier transform infrared (FTIR), and X-ray absorption fine structure (XAFS) spectroscopies. For UV–Vis analysis, water was transferred to a quartz cuvette, and absorbance was recorded in the range 200–800 nm on a Hewlett-Packard 8453 spectrophotometer. All spectra were normalized to solution DOC concentrations to yield absorptivity units (L mg-C^{-1} m^{-1}). Indices commonly used to examine aromaticity and humification were calculated, including specific ultraviolet absorptivity at 254 nm ($SUVA_{254}$) (Weishaar et al. 2003; Stolpe et al. 2013), and the ratio of absorptivity at 265 nm to 465 nm ($A_{265/465}$) (Chen et al. 2002). $SUVA_{254}$ was corrected to remove Fe absorbance using an equation modified from Weishaar et al. (2003): $y = 0.78\ x + b$, where y is the measured absorbance (cm^{-1}), x is the mass ratio of Fe to DOC, and b is the absorbance (cm^{-1}) when Fe/DOC = 0. Values for b were used to calculate $SUVA_{254}$ for each sample.

Fourier transform infrared (FTIR) spectra were obtained on a Nicolet Magna 760 spectrophotometer equipped with a liquid nitrogen cooled MCT (Hg-Cd-Te) detector (Chen et al. 2002). Solutions were deposited on ZnSe windows and dried in an oven at 60 °C prior to analysis. For extracts with low DOC concentrations, samples were concentrated by depositing multiple layers on the window. All spectra were background corrected against a clean ZnSe window. The wavenumbers (cm^{-1}) and relative intensities of absorbance peaks were determined following baseline subtraction using Thermo Nicolet OMNIC v7.3 software. Indices examined include the ratios of maximum absorbance in regions representing hydroxyl O–H (3300–3400 cm^{-1}), aliphatic C–H ($\sim$2935 cm^{-1} and 1400 cm^{-1}), carbonyl C=O ($\sim$1740 cm^{-1}), aromatic-C and conjugated carboxylate C=O (1590–1650 cm^{-1}), and polysaccharide C–O (1030–1070 cm^{-1}) functional groups (Solomon et al. 2005).

Fluorescence-yield Fe K-edge EXAFS spectra were measured at beam line 7-3 at the Stanford Synchrotron Radiation Lightsource using a variable-exit geometry Si(220) double-crystal monochromator. Soil pore water and ferrihydrite suspensions were loaded into plastic sample holders with Kapton windows, frozen in LN, and mounted in a LHe cryostat. Data were measured with the samples maintained at <10 K to minimize photo-initiated chemical changes to the samples (none observed). Harmonics were rejected using a Rh-coated silicon mirror. Fluorescence-yield data were collected using a 32-element germanium array detector. XAFS spectra were processed using SIXPACK (Webb 2005).

For C XANES (X-ray absorption near edge structure), soils were ground in an agate mortar and pestle and slurried in ultrapure water. Soil suspensions and pore waters were deposited onto In foil or Au-coated Si wafers and air-dried at room temperature. The wafers were then affixed to sample holders using double-sided carbon tape, and fixed onto a multi-axis sample manipulator in the X-ray absorption vacuum chamber. XANES spectra were collected using the Spherical Grating Monochromator (SGM) beamline 11ID-1 at the Canadian Light Source (CLS, Saskatoon, Saskatchewan, Canada). The beamline delivers 10^{11} photons s^{-1} at the C *K*-edge, with a resolving power (E/ΔE) >10,000 (Regier et al. 2007a, b). Spectra were acquired using the slew scanning mode of the SGM beamline which continuously scans the energy of the monochromator while acquiring data in order to minimize X-ray exposure. Each slew scan took 20 s and multiple, unique spots were scanned on each sample. The beamline exit slit was set at <25 μm and fluorescence yield data was collected using an array of Amptek silicon drift detectors (SDD). The detectors were positioned at 90 degrees with respect to the incident beam in the plane of polarization. For calibration at the C *K*-edge, a solid-state absorption spectrum for citric acid was measured. Ten scans from unique locations on the sample were averaged together. To normalize the resulting spectrum against the beamline flux (I_0), it was divided by the elastic scattering signal obtained from a freshly deposited gold-coated Si wafer. The resulting XANES data were processed using custom macros in IGOR Pro. Spectra were deconvoluted following the procedure of Solomon et al. (2005).

Statistics

Statistical analyses were performed in Origin® software (OriginLab). One-way analysis of variance

(ANOVA) and the Tukey test for means comparison were used to test the effect of depth (binned as surface (=0 cm), shallow (0–7 cm), intermediate (18–35 cm), or deep (>35 cm)) or sampling date (early July or late August) on concentrations of dissolved species in surface and soil water. Effects of depth, polygon type, microtopographic feature, and sampling date on concentrations of dissolved gases were also tested with ANOVA. The effects of polygon type and microtopographic feature on dissolved ions were not determined in this study because these factors were previously evaluated using a more comprehensive dataset (Newman et al. 2015). Linear regression was used to evaluate significant correlations between dissolved species. Any p-values <0.05 were considered significant for all tests.

Results

Water and soil chemistry

Surface soils at center locations of the transitional and low-centered polygons remained water saturated from July to August, while those of the flat and high-centered polygons were unsaturated (Fig. S1). Soil moisture recorded above the water table (<10 cm) decreased from the transitional > low-centered > flat-centered > high-centered polygons, consistent with relative soil moisture regimes reported for each polygon type (Lara et al. 2014). Average thaw depth measured across all areas in 2012–2014 increased from July (23 ± 4 cm), August (42 ± 5 cm), to September (50 ± 8 cm), similar to trends reported previously for the BEO (Shiklomanov et al. 2010; Hubbard et al. 2013).

Concentrations of individual solutes and statistical analysis of their variation with depth are provided in the supporting information (Table S1 and Fig. S3, respectively) and in an online database (Herndon et al. 2015b). Here, we summarize the chemical properties of surface and soil water and evaluate specific analytes of interest. Surface and shallow soil pore waters were chemically similar and more dilute (electrical conductivity, EC = 210 ± 20 μS cm^{-1}) than those from intermediate and deep soils (EC = 464 ± 33 μS cm^{-1}) ($p < 0.001$). Water pH was slightly acidic (=5.9 ± 0.6, averaged over all samples) and did not vary with depth (Fig. 2 and S3). Soil water was organic-rich, and DOC concentrations increased from the surface (4.8 ± 1.1 mmol L^{-1}) to intermediate and deep soils (15 ± 2 mmol L^{-1}) ($p < 0.001$). Several low-molecular weight organic acids (acetate, formate, propionate, butyrate) were detected in soil water (Fig. 3). Acetate and propionate were low in the surface and shallow waters but peaked in the middle of the active layer and decreased from early July to late August.

The potential terminal electron acceptors in soil solution were dominated by Fe(III), with an average concentration of 0.37 ± 0.10 mmol L^{-1} across all sampled water (Table S1). Other potential electron acceptors were much lower, with SO_4^{2-} averaged at 0.07 ± 0.01 mmol L^{-1} and NO_3^- at 0.03 ± 0.02 mmol L^{-1} (Table S1). Fe(III) concentrations were low near the land surface and peaked in the middle of the active layer where Fe(III) comprised ~60 % of total dissolved Fe (Fe_{TOT}) (Fig. 2; $p < 0.001$)). Fe(II) increased with depth and comprised ~70 % of Fe_{TOT} in deep soils ($p < 0.001$). Sulfate concentrations were relatively low but also exhibited a vertical gradient, increasing from surface and shallow soils (0.03 ± 0.01 mmol L^{-1}) to intermediate and deep soils (0.12 ± 0.01 mmol L^{-1}) ($p < 0.001$). Nitrate concentrations were variable with depth and slightly elevated near the surface, with the highest value (0.57 mmol L^{-1}) measured in the unsaturated soil pore water of the HCP. For comparison, all other sampled waters contained $NO_3^- < 0.08$ mmol L^{-1}. The depth profiles of non-redox sensitive elements (e.g., Cl) exhibited similar trends, increasing by factors of <3X from the surface to deep soils (Fig. 2; Table S1). Phosphate concentrations were near or below the detection limit (<1 μmol L^{-1}) (Table S1).

Depending on where the soil cores were collected, the organic horizons reached to a depth of 8–30 cm before the mineral horizons began. The boundary of these two distinct horizons varied by ~20 cm but generally aligned with intermediate depth of the active layer (Fig. S2). In bulk soil collected from the LCP, Fe concentrations were higher in the organic horizons (359 ± 6 mmol kg^{-1}) than in the mineral horizons (225 ± 58 mmol kg^{-1}) (Table 1). In contrast, Na concentrations were low in the organic horizons (135 ± 80 mmol kg^{-1}) relative to mineral horizons (292 ± 18 mmol kg^{-1}). Ratios of Fe to the relatively immobile element Ti were higher in the organic horizons (Fe/Ti >11) than the mineral horizons (Fe/Ti <5). Ratios of other inorganic elements (Na, K,

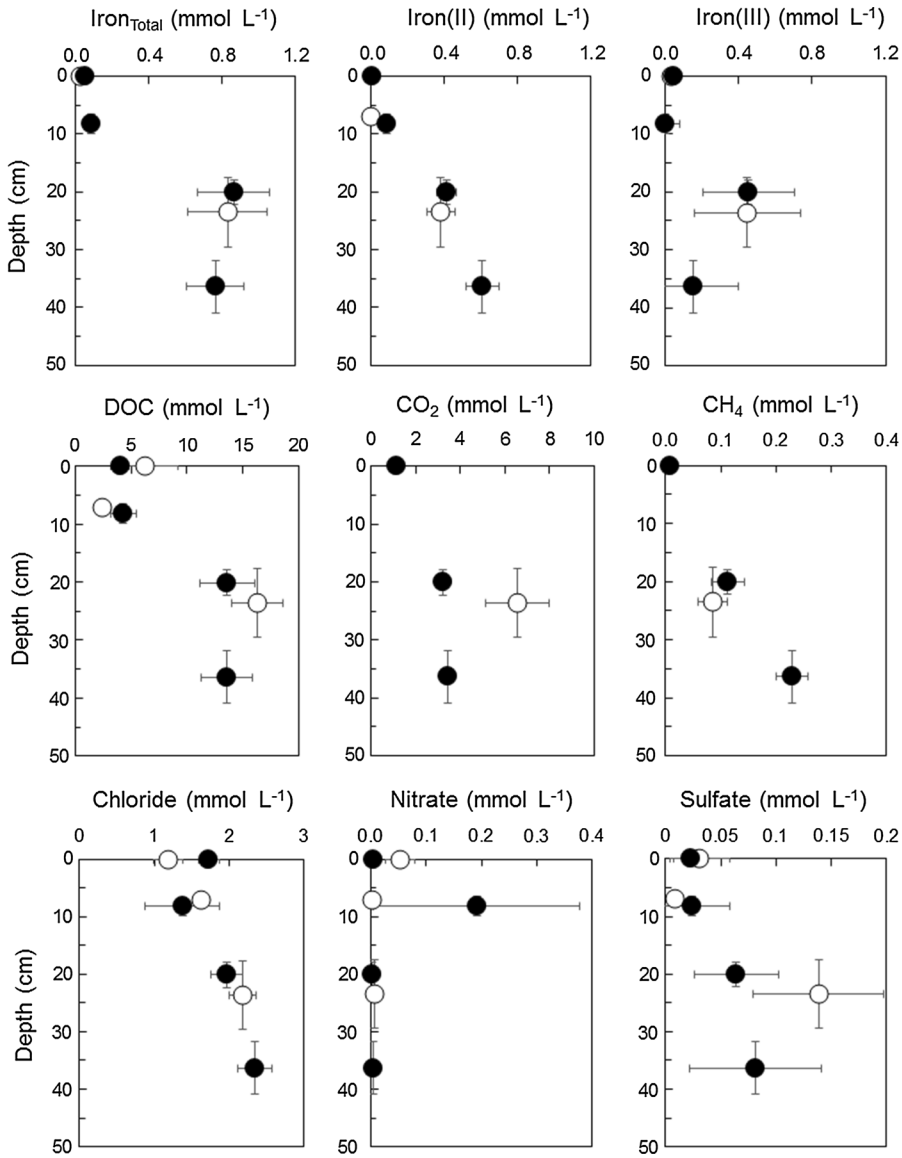

Fig. 2 Average concentrations (± standard error) of dissolved iron species, anions, dissolved organic C (DOC), and dissolved gases (CO_2 and CH_4) in tundra pore waters in early July 2013 (*open circle*) and late August 2013 and 2014 (*closed circle*). Sample data from all polygon sites for each collection month were used in the average. Each depth interval was binned as surface, shallow, intermediate, or deep soil water. Note that the concentration scale varies in each plot

Mg, Al, Mn, Ca) to Ti were relatively similar across all depths (Table 1).

Spatial and temporal patterns of dissolved gases

Concentrations of dissolved CO_2 and CH_4 in surface waters were 1.3 ± 0.1 mmol L^{-1} and 0.008 ± 0.005 mmol L^{-1}, respectively (Table S1). The CO_2 value is 100 times higher than that in equilibrium with 400 ppm atmospheric CO_2, demonstrating high productivity in the thawed soil. Dissolved CO_2 and CH_4 increased with depth (Table 2) but exhibited different seasonal patterns in saturated soils (Fig. 2). Methane concentrations were higher in deep soils (0.27 ± 0.05 mmol L^{-1}) than in intermediate soils (0.10 ± 0.03 mmol L^{-1}) and did not vary between July and August (Fig. 2; Table 2). In contrast, CO_2 concentrations decreased from early July (6.6 ± 1.4 mmol L^{-1}) to late August (2.8 ± 0.2 mmol L^{-1}) in intermediate soil depths but did not increase from intermediate to deep soils (Fig. 2; Table 2). Consequently, molar ratios of CH_4:CO_2 increased with depth in the soil ($p < 0.001$) but did not change significantly from July to August. Polygon classification and topographic position were

not significant factors influencing dissolved CO_2 and CH_4 concentrations ($p > 0.05$; Table 2); however, the highest dissolved CH_4 concentrations (>0.25 mmol L^{-1}; $+1\sigma$) were observed in the LCP.

Dissolved CH_4 was strongly positively correlated with Fe_{TOT} (Fig. 4a) with the exception of one site (the trough in area C) that had consistently high Fe_{TOT} but low CH_4. Dissolved CH_4 was not significantly correlated ($p > 0.05$) with the proportion of Fe(III)/Fe_{TOT} across all sites. Rather, at intermediate depths in transitional and LCP soils, CH_4 increased with increasing Fe(III)/Fe_{TOT} ($p < 0.001$), while the opposite trend was observed in the flat- and HCP ($p < 0.05$) (Fig. 4b). In pore water near the permafrost boundary, CH_4 concentrations were high but Fe(III)/Fe_{TOT} was variable. These observations contradict the expectation that CH_4 would be low where Fe(III) is abundant due to inhibition of methanogenesis by Fe(III)-reduction reactions.

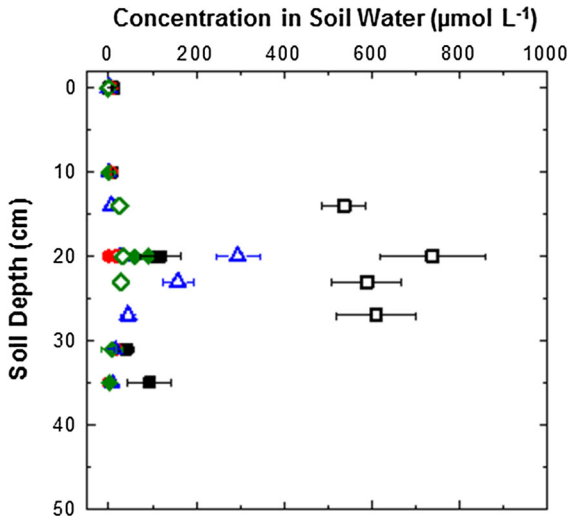

Fig. 3 Concentrations (± standard error) of acetate (*closed square*), formate (*closed circle*), propionate (*closed triangle*), and butyrate (*closed diamond*) in soil pore water collected in early July (*open symbols*) and late August (*closed symbols*) 2014 are plotted versus soil depth

Spectroscopic characterization of carbon and iron

Fe K-edge EXAFS spectra of pore water samples collected from the middle of the active layer (NGEE_32; 25 cm depth) and from near the permafrost boundary (NGEE_33; 43 cm depth) in the trough of a low-centered polygon (area A) in late August 2013 are similar to that of ferrihydrite suspended in 2 mM Elliot soil humic acid (Fig. 5b). All spectra show a strong Fe–O pair correlation in the Fourier Transforms (FTs) at ca 1.5 Å (R + dR) (Fig. 5c), which corresponds to an interatomic distance of ca 2.00 Å (Karlsson and Persson 2012). Peaks and valleys (positive and negative antinodes) in the EXAFS spectra at 4, 5.2, 6.2, 7 and 8.4 $Å^{-1}$ correspond to this pair. The FT for ferrihydrite exhibits Fe–Fe pair correlations at ca 2.8 and 3.1 Å (R + δR),

Table 1 Elemental concentrations (mmol kg^{-1}) and ratios of mobile elements to the immobile element Ti in bulk soil samples from the organic or mineral horizon of the low-centered polygon (area A)

Sample ID	Position	Horizon	Depth (cm)	Fe	Al	Ca	K	Mg	Na	Si	Mn	P	Ti
NGADG0005-1	Ridge	Organic	0–8	355	632	80	86	92	78	2690	0.31	25	22
NGADG0009-1	Trough	Organic	0–19	364	897	59	150	105	191	8250	0.44	19	32
NGADG0005-2	Ridge	Mineral	8–46	162	1050	53	167	105	283	11,100	0.42	10	41
NGADG0009-2	Trough	Mineral	25–69	203	965	61	165	98	290	12,700	0.62	12	43
NGADG0002-2	Trough	Mineral	7.5–49.5	235	1220	59	207	129	318	13,300	0.68	11	49
NGADG0017-2	Center	Mineral	21.5–53.5	300	1410	75	235	167	277	10,300	0.98	14	61

Sample ID	Position	Horizon	Depth	Fe/Ti	Al/Ti	Ca/Ti	K/Ti	Mg/Ti	Na/Ti	Si/Ti	Mn/Ti	P/Ti
NGADG0005-1	Ridge	Organic	0–8	16.1	28.7	3.6	3.9	4.2	3.6	122	0.014	1.1
NGADG0009-1	Trough	Organic	0–19	11.5	28.3	1.9	4.7	3.3	6.0	260	0.014	0.6
NGADG0005-2	Ridge	Mineral	8–46	3.9	25.6	1.3	4.1	2.6	6.9	269	0.010	0.3
NGADG0009-2	Trough	Mineral	25–69	4.7	22.5	1.4	3.9	2.3	6.8	295	0.014	0.3
NGADG0002-2	Trough	Mineral	7.5–49.5	4.8	24.8	1.2	4.2	2.6	6.5	271	0.014	0.2
NGADG0017-2	Center	Mineral	21.5–53.5	4.9	23.2	1.2	3.9	2.7	4.6	170	0.016	0.2

Analytical error is ±3 %

Table 2 Statistical tests (ANOVA) on spatial and temporal patterns of dissolved gases in surface and soil water at significance levels of $p < 0.05$ (*), $p < 0.01$ (**), and $p < 0.001$ (***)

	Dissolved CO_2	Dissolved CH_4	CH4:CO2
Depth interval[a]	**	***	***
Sampling date[b]	***	n.s.	n.s.
Polygon site[c]	n.s.	n.s.	n.s.
Microtopographic feature[d]	n.s.	n.s.	n.s.

Not significant (n.s.) results had $p > 0.05$

[a] Binned as surface, shallow, intermediate, or deep

[b] Binned as early July or late August

[c] Transitional, low-centered, flat-centered, or high-centered polygon

[d] Trough, ridge, or center

attributed to Fe–Fe interatomic distances of 2.98 and 3.41 Å (Karlsson and Persson 2012). Distinctive positive antinodes in the EXAFS spectra at ca 5.2 and 7.4 $Å^{-1}$ are characteristic of these Fe–Fe pairs. Both of the 5.2 and 7.4 $Å^{-1}$ EXAFS features are present in the NGEE_33 pore water sample, but at much weaker amplitude than in ferrihydrite (Fig. 5b). In the NGEE_32 sample, this feature is only weakly present. This diminution of amplitude previously has been shown to occur when ferrihydrite is present in natural waters as an equal or minor component along with Fe(III)-organic matter complexes (Karlsson and Persson 2010, 2012; Karlsson et al. 2008). The FTs of both pore water samples contain a shoulder on the low-R side of the 2.8 Å feature (Fig. 5c), consistent with the presence of Fe(III)-carboxylate coordination environments. In summary, the EXAFS spectra suggest that both Fe(III) oxides and Fe(III)-OM complexes are present in the pore waters, with sample NGEE_32 having the lowest apparent concentration of Fe(III) oxides. These results mirror the proportions of DOC and Fe measured in pore water. Specifically, water from the middle of the active layer (corresponding to NGEE_33) contained ~19X more DOC than Fe, whereas water from the deep mineral soil (corresponding to NGEE_32) contained only ~9X more DOC than Fe.

Pore water $SUVA_{254}$, a proxy for aromaticity (Weishaar et al. 2003), increased from the surface to the middle of the active layer and was highest in late August ($SUVA_{254} = 6.0 \pm 0.8$ L mg-C^{-1} m^{-1}) (Fig. 6a). However, $SUVA_{254}$ was low in pore waters from deep soils (2.8 ± 0.8 L mg-C^{-1} m^{-1}), and the lowest values (<1.2) occurred at the deepest depths. Similarly for water samples analyzed with FTIR ($n = 32$), proportions of aromatic-C (+ conjugated C=O) to aliphatic-C were constant (1640/1400 peak ratio $= 1.7 \pm 0.1$) in samples at all depths and polygons. In contrast, hydroxyl and polysaccharide C-O groups varied by 25–53 % in these samples, and their proportion relative to aromatic-C (1640/3300 $= 0.83 \pm 0.21$ and 1640/1040 $= 2.0 \pm 1.1$) was lower in the surface and deep layers relative to the middle of the active layer, which contains fewer minerals and exhibited higher proportions of dissolved aromatic-C (Fig. 6b). This result is consistent with increases in $SUVA_{254}$ (Fig. 6a).

The relative abundance of different organic functional group character (aromatic, phenolic, aliphatic, carboxylic, and alkyl) in pore water DOC and bulk soil SOC was evaluated with C XAFS (Fig. 5a). DOC was relatively enriched in carboxyl functional group character relative to SOC. In contrast, SOC was relatively enriched in functional groups having aliphatic and aromatic character. These results further support the preferential sorption of aromatic-rich compounds to minerals in the deep layer, and the trends also reflect the higher solubility of oxygen-rich compounds than hydrophobic aromatic and aliphatic compounds. SOC and DOC were distinct from humic acid and tannic acid reference compounds (Fig. 5a), indicating a relative lack of humification in the Arctic soils.

Discussion

Depth gradients in water chemistry

Water chemistry in the thaw season is characterized by vertical gradients with solute concentrations that

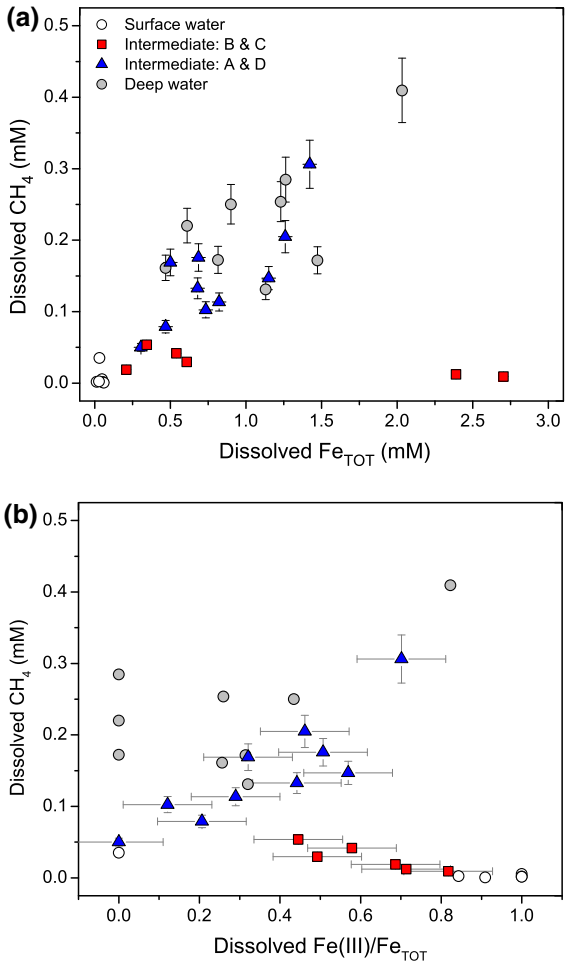

Fig. 4 **a** Concentrations of dissolved CH_4 (mM) increased with increasing dissolved Fe_{TOT} (mM) in surface water and soil pore water ($p = 0.05$). Excluding one site (the trough in the flat-centered polygon) that had high Fe_{TOT} but low CH_4 concentrations in both July and August, the correlation between dissolved CH_4 and Fe_{TOT} was highly significant ($p < 0.001$). **b** CH_4 increased with increasing $Fe(III)/Fe_{TOT}$ in soil waters from intermediate depths in the low-centered and transitional polygons (blue triangles; $R^2 = 0.71$, $p = 0.001$) but decreased with increasing $Fe(III)/Fe_{TOT}$ in the drier flat- and high-centered polygons (*red squares*; $R^2 = 0.74$, $p < 0.05$). Deep soil pore waters (*grey circles*) had variable $Fe(III)/Fe_{TOT}$ and high CH_4, while surface waters (*open circles*) had variable $Fe(III)/Fe_{TOT}$ and low CH_4 ($p > 0.05$). Error bars are omitted from deep and surface water symbols for clarity

generally increase with increasing depth. Although geochemical characterization of Arctic tundra remains limited, our results are consistent with previous observations that solute chemistry varies significantly with depth in the active layer (Brown 1969; Kokelj and Burn 2005; Newman et al. 2015). Solute concentrations may increase near the permafrost boundary due to mineral dissolution or chemical weathering driven by increased water availability (e.g., Lacelle et al. 2008), solute exclusion during downward freezing (e.g., Kokelj and Burn 2005), or inputs of ion-rich waters from depth during periodic thawing of the upper permafrost (Kokelj and Burn 2003). Regardless of the process that concentrates ions at depth, which remains unclear for this system (Newman et al. 2015), simple diffusion cannot fully explain vertical gradients for all solutes in this study given that geochemical gradients are high for redox-active elements (e.g., Fe, S) but low for conservative elements (e.g., Na, Cl).

Biogeochemical processes, e.g., microbial-mediated oxidation and reduction reactions, likely drive prominent vertical gradients for redox-sensitive elements. Distinct microbial processes may occur along steep redox gradients and alter Fe chemical speciation. Fe(II) concentrations are highest at depth whereas Fe(III) peaks in the middle of the active layer, and little dissolved Fe is present near the soil surface (Fig. 2). We infer from low concentrations of sulfate in shallow pore waters (Fig. 2) that minor sulfate-reduction may be occurring primarily at depths <20 cm. DOC that is produced from microbial decomposition reactions may also complex metal ions (e.g., Fe, Al, Ca, Mg) and redistribute them within the soil profile, resulting in vertical concentration gradients (Fig. S3). Differences between geomorphic features were not evaluated in this study; however, Newman et al. (2015) and Wainwright et al. (2015) report greater geochemical differences amongst polygons rather than features at these sites.

Water chemistry is especially dynamic in the middle of the active layer near the boundary between organic and mineral horizons, possibly due to progressive lowering of the water table during the thaw season that also increases the depth of the oxidation front. The redox gradients generated by water table fluctuations and microtopographic features on the landscape control Fe geochemistry, which in turn impacts microbial decomposition of SOM and release of C to the atmosphere. As detailed below, we propose a conceptual model for Fe cycling at our study sties (Fig. 7) which provides a framework for understanding biogeochemical processes in anoxic, Fe-rich tundra soils.

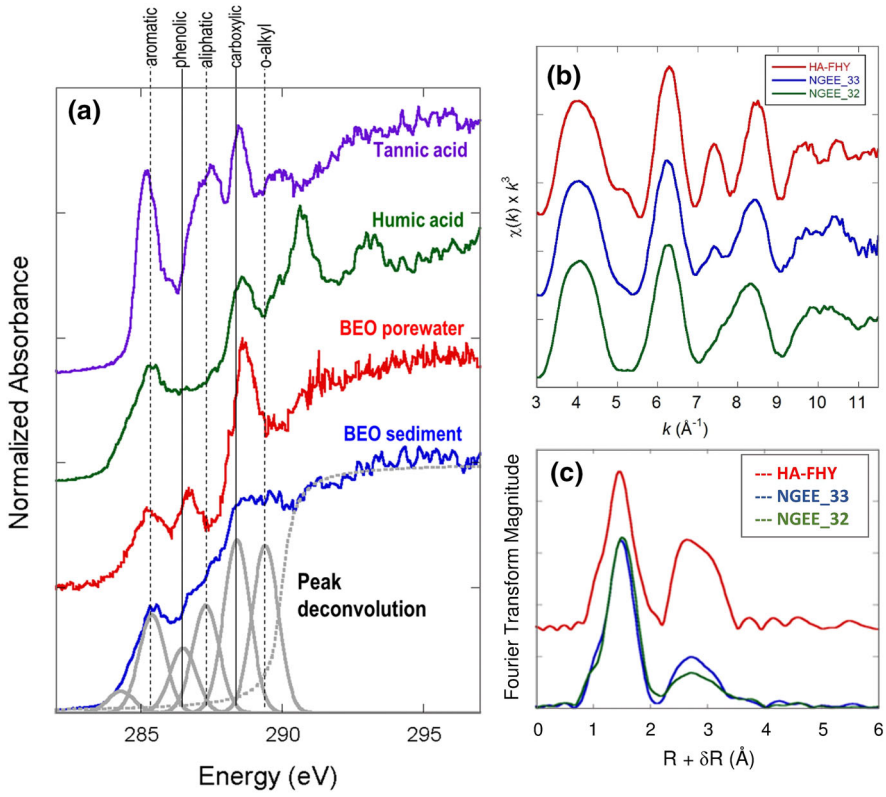

Fig. 5 **a** Representative carbon K-edge NEXAFS spectra for pore water (*red*) and soil (*blue*) samples collected from the BEO. Dissolved organic carbon in tundra pore water was enriched in carboxyl groups relative to the solid-phase organic matter (*blue*), which was conversely relatively enriched in groups exhibiting aromatic and aliphatic character (Solomon et al. 2005). Spectra for tannic acid and humic acid reference standards, shown for comparison, are distinct from the sample spectra. **b** Iron K-edge XAFS spectra for pore water samples collected the middle of the active layer (NGEE_32; 25 cm depth) and from the permafrost boundary (NGEE_33; 43 cm depth) in the trough of a low-centered polygon (area A) in late August 2013. A reference spectrum for a humic acid + ferrihydrite solution (HA-FHY) is shown in *red*. **c** Decreased amplitude of the Fe–Fe scattering peak of NGEE_32 relative to NGEE_33 in the Fourier Transform suggests a higher proportion of Fe(III) complexed with DOC relative to ferrihydrite

Iron cycling and Fe–C interactions in the active layer

Concentrations of dissolved Fe(III) are highest in the middle of the active layer, while Fe(II) concentrations are highest in deep soils (Fig. 2). Fe(III) is only sparingly soluble at circumneutral pH, thus its high concentrations (up to 2 mmol L^{-1}) are indicative of the presence of particulate iron oxide stabilized by DOM (Liang and Morgan 1990; Liang et al.1993) or Fe(III)-DOC complexes in soil pore waters. As determined from x-ray absorption spectra (Fig. 5a, b), Fe(III)-OM complexes are more prevalent in the middle of the active layer where DOM:Fe ratios are higher than in deeper soils. Pore waters in the middle of the active layer contain high concentrations of DOC and a high proportion of dissolved aromatic-C (Fig. 6), likely derived from the decomposition of plant material in the organic layer. These compounds enhance Fe solubility by complexing Fe(III) that is present in the organic horizon (Fig. 7). DOM in the deeper mineral soils is relatively depleted in aromatic-C, which can be attributed to the preferential adsorption of aromatic-C on minerals such as iron oxides (Fig. 7) (Gu et al. 1995, 1996).

High Fe/Ti ratios in the organic horizon indicate that Fe in the shallow soils is present as iron oxide precipitates or iron-OM complexes (Fig. 7) rather than primary minerals that input through cryoturbation, as previously suggested for adjacent drain thaw lake basins (Lipson et al. 2013). If Fe in the organic horizon was present in primary minerals, then ratios of Fe to

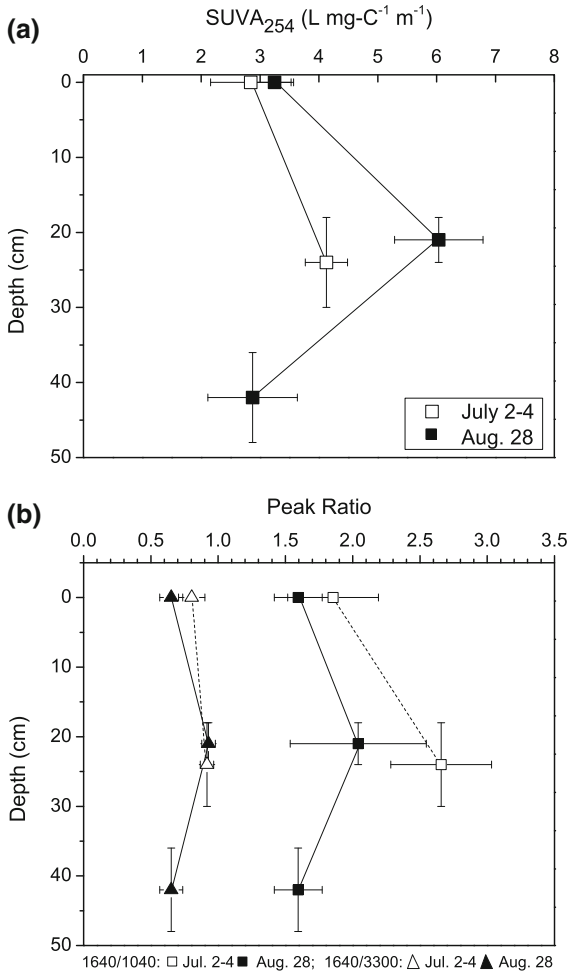

Fig. 6 **a** $SUVA_{254}$ (L mg-C^{-1} m^{-1}) of DOC in surface and pore waters peaked in the middle of the active layer and was low at depth. **b** Infrared absorbance at 3300 and 1040 cm^{-1}, indicative of O–H and polysaccharide C–O functional groups, respectively, decreased relative to C=C + C=O absorbance at 1640 cm^{-1}, consistent with $SUVA_{254}$ measurements in (**a**). *Symbols* and *error bars* indicate the average and standard error across all measurements at each depth

the relatively immobile element Ti would be similar to those of Na/Ti in the organic and mineral horizons. Na is considered a conservative element because it does not accumulate in plant biomass or precipitate in secondary minerals after release from mineral weathering; therefore, Na in the organic horizon was likely hosted in primary minerals that were transported from the mineral horizon during cryoturbation. Although ratios of most rock-derived elements (Na, K, Mg, Al, Mn, Ca) to Ti were relatively similar across all depths (Table 1), Fe/Ti was >11 in the organic soils and <5 in the mineral soils. Only phosphorus, an element that is taken up by plant and accumulates in organic matter, exhibited a similar pattern to Fe. It is important to note that the area-normalized mass of each element (mmol m^{-2} $horizon^{-1}$), including Fe, is expected to be higher in the mineral horizon than the organic horizon given that the mineral horizon has a greater bulk density (e.g., Bockheim et al. 2003).

It is likely that microbial reduction of Fe-oxides in the mineral horizon generate Fe(II), which is diffused upward in the soil and subsequently oxidized, forming iron oxyhydroxide colloids or Fe(III)-DOM complexes (Fig. 7) (Liang et al. 1993). Redistribution of Fe from deep mineral soils towards the shallow organic horizons should stimulate microbial activity by providing microorganisms with a terminal electron acceptor for anaerobic respiration. This interplay of microbial solubilization/reduction of Fe(III) and vertical transport, followed by chemical oxidation of Fe(II), may also serve as a mechanism to replenish Fe(III) in the deep soils. For example, in persistently anoxic soils at depth, depletion of Fe(III) and accumulation of Fe(II) during the thaw season will slow down Fe-reduction and SOM fermentation process (Lipson et al. 2012). However, Fe(III) can be replenished in the deep soils if Fe(III)-rich water flows downwards as thaw depth increases over thaw season.

Fe-oxyhydroxide precipitation in the organic horizon may also impact the bioavailability of plant nutrients. For example, phosphorous solubility is limited by adsorption to Fe-oxyhydroxide minerals (Jensen et al. 1992; Rentz et al. 2009). In these tundra soils, P is strongly correlated with Fe in bulk soils ($R^2 = 0.7$, $p = 0.02$) while dissolved PO_4^{3-} concentrations are low (<1 μmol L^{-1}). Recent studies suggest that climate projection models overestimate the potential of terrestrial biomes to sequester carbon because they do not consider nutrient constraints (Wieder et al. 2015); however, the potential for Fe precipitates to limit the pool of bioavailable P in the arctic remains unclear. Our research provides evidence that surface organic horizons contain Fe(III) precipitates that may provide reactive surface area for adsorption of phosphate.

Spatial gradients of carbon dioxide and methane

The result that dissolved CO_2 decreases, but CH_4 and CH_4:CO_2 ratios remain constant from early July to late August supports a scenario where CO_2 is generated

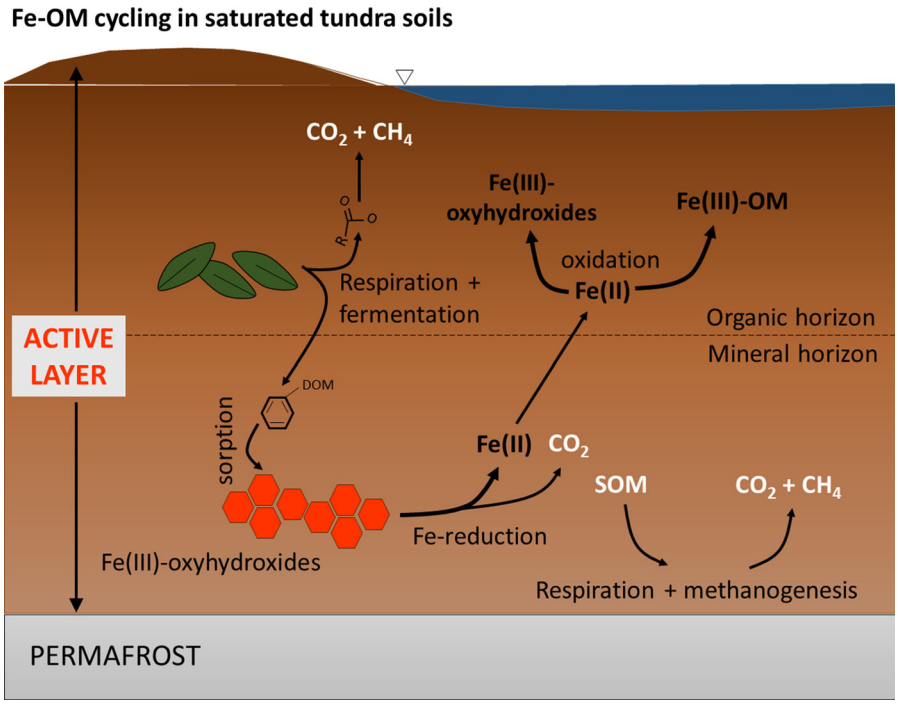

Fig. 7 Conceptual model of Fe and organic matter cycling in saturated tundra soils presented as a cross-sectional view of an idealized tundra active layer in a low-centered polygon. The diagram shows components of Fe cycling that include reduction of iron oxides, diffusion of soluble Fe species, and oxidation of soluble Fe to form Fe(III)-oxyhydroxides and organic-bound Fe(III). Components of C cycling shown include decomposition of plant matter, sorption of aromatic DOM to iron mineral surfaces, and production of carbon dioxide and methane via respiration, fermentation, and acetoclastic methanogenesis pathways

from fermentation and respiration (root + microbial) immediately following the thaw while methanogenesis increases as the season progresses (Fig. 7). High concentrations of acetate, which is produced by fermentation and consumed in acetoclastic methanogenesis, are present in pore waters collected from near the organic-mineral horizon boundary, while low concentrations are present near the surface and at depth (Fig. 3). Acetoclastic methanogenesis is the dominant CH_4 producing pathway across the BEO (Throckmorton et al. 2015), and decreasing concentrations of acetate from July to August may be attributed to decreasing production via fermentation and increasing consumption to produce CO_2 and CH_4. Similar trends were observed in anoxic incubations of LCP soils, in which organic acids initially accumulated before being consumed to generate CH_4 (Roy Chowdhury et al. 2015; Herndon et al. 2015a).

While CO_2 increases only slightly with depth, dissolved CH_4 concentrations increase sharply and are highest (up to 0.4 mmol L^{-1}) near the permafrost boundary at all sites (Fig. 2). Methane concentrations vary with soil moisture in the middle of the active layer; that is, CH_4 concentrations are high in transitional and low-centered polygons where soils remain saturated at the surface but low in flat and high-centered polygons that experience seasonal drying (Fig. 4b). Our results support observations by Wainwright et al. (2015) that CH_4 efflux is high from LCP soils but low from HCP and FCP soils, regardless of topographic position. Methane concentrations at depths >20 cm exceed concentrations reported for shallow inundated soils (<0.1 mmol L^{-1}) in an adjacent drained thaw lake basin (Lipson et al. 2012; Miller et al. 2015), indicating that measurements of CH_4 near the soil surface (<15 cm) significantly underestimate total production within the thawed soils. Although CH_4 losses can be mitigated by aerobic oxidation of CH_4 to CO_2 during diffusion through an oxic surface layer (Moosavi and Crill 1998; Pearce and Clymo 2001), dissolved gases

that are produced in anoxic subsurface soils can be released to the atmosphere through plant aerenchyma tissue (Shannon and White 1994; von Fischer et al. 2010) or following lateral diffusion into nearby lakes (Paytan et al. 2015). In fact, recent studies at the BEO indicate that <3 % of CH_4 is oxidized in surface soils; rather, CH_4 that is produced in the subsurface is chiefly transported to the atmosphere through ebullition and aerenchyma transport (Throckmorton et al. 2015). Other studies indicate that CH_4 efflux increases with thaw depth (Sturtevant and Oechel 2013; Kim 2015) and is enhanced by higher soil temperatures and greater evaporative losses in areas where the water table is above the land surface, e.g., the transitional and low-centered polygons (Turetsky et al. 2008; Zona et al. 2012; Liljedahl et al. 2012). Our results provide measurements of CH_4 at depth that may be used to understand production pathways and sources of CH_4 efflux.

Influence of Fe geochemistry on microbial production of CO_2 and CH_4

Given that methanogens require anoxic conditions and low redox potentials, methanogenesis may be limited in soils with abundant Fe-oxides (e.g. ferrihydrite) or organic-bound Fe(III) that can act as terminal electron acceptors. Consistent with expectations, CH_4 decreases with increasing Fe(III)/Fe_{TOT} in the flat- and HCP (Fig. 4b). Similar trends were observed for shallow pore waters (<15 cm depth) in nearby drained thaw lake basins (Lipson et al. 2012). In contrast, CH_4 increases with increasing Fe(III)/Fe_{TOT} in the persistently-saturated transitional and LCP, and the highest CH_4 concentrations are observed at sites with >50 % Fe_{TOT} as Fe(III).

It was expected that CH_4 concentrations would be low in areas where Fe(III) concentrations are high given that Fe-reduction reactions yield more energy than methanogenesis in many environments and hinder methane production due to competition for substrates (Bond and Lovley 2002; Metje and Frenzel 2007; Lipson et al. 2012). However, differences in mineralogy of the colloidal Fe(III) may explain differences in CH_4 and Fe(III) correlation between sites. In the flat and HCP regions, surface soils become oxidized as the water table lowers over the thaw season (e.g., Lipson et al. 2013), favoring the precipitation of short-range order ferrihydrite minerals. Ferrihydrite may suppress methanogenesis by serving as an energetically favorable terminal electron acceptor (Roden and Wetzel 1996; Bethke et al. 2011); thus, CH_4 decreases with increasing Fe(III) (Fig. 4b). Transitional and low-centered polygon soils may contain more crystalline minerals (e.g. magnetite and hematite) relative to ferrihydrite due to persistently reducing conditions that favor the formation of crystalline minerals and depletion of ferrihydrite (Lovley et al. 1987; Lovley and Phillips 1988; Hansel et al. 2003; Weber et al. 2006). These crystalline iron oxides serve as poor electron acceptors for anaerobic respiration and may not hinder methane production.

However, this reasoning cannot fully explain positive correlations between dissolved methane and total and oxidized Fe (Fig. 4). Alternatively, certain crystalline Fe minerals may enhance methanogenesis by providing a conduit for electron transfer (Kato et al. 2012). Lipson et al. (2010) provide evidence that deep mineral soils in a nearby drained thaw lake basin contain crystalline iron oxides including magnetite. Magnetite is a poor terminal electron acceptor for Fe-reduction (Lovley and Phillips 1988) but can serve as both a sink and source of electrons (Byrne et al. 2015) and thus facilitate electron transfer and methane production from organic substrates (Kato et al. 2012); consequently, CH_4 increases with increasing Fe(III) (Fig. 4b). This scenario implies that Fe-oxide mineralogy may be a dominant factor regulating methanogenesis in tundra soils; however, more studies are needed to characterize Fe-oxide mineralogy at these sites to confirm these hypotheses.

Conclusions

Our results indicate that Fe redox cycling and vertical transport impact organic matter degradation in anoxic tundra soils. Spatial and temporal variability in water saturation generate geochemical gradients that control Fe speciation, which in turn influences microbial production of carbon dioxide and methane from carbon substrates in the soil. Fe-reduction deep in the mineral horizon of the active layer produces Fe(II) that diffuses upwards in the soil profile and is oxidized to iron oxyhydroxide minerals and organically-complexed Fe(III) in the organic horizon. Enrichment of oxidized Fe influences organic matter decomposition by providing an abundant terminal electron acceptor for

microbial decomposition reactions, providing reactive mineral surfaces that sorb organic compounds and the limiting-nutrient phosphorus, and facilitating electron transfer that may enhance methanogenesis. We contend that Fe cycling will become increasingly important to C fluxes as warming temperatures thaw mineral horizons that underlie surface organic layers. It is necessary to consider the impacts of iron geochemistry on substrate availability and greenhouse gas production in order to predict future changes in C storage and releases of CO_2 and CH_4 from arctic ecosystems.

Acknowledgments The authors would like to thank Kenneth Lowe for core sample collection, and Taniya Roy Chowdhury, Xiangping Yin, Benjamin Mann, Tonia Mehlhorn, Sharon Bone, Jay Dynes, Margaret Murphy, and Henry Gong for technical assistance and chemical analyses. All data are available in the supporting information for this manuscript and in an online data repository (NGEE-Arctic Data Portal). The Next Generation Ecosystem Experiments (NGEE-Arctic) project and the SLAC Science Focus Area (SFA) program are supported by the US Department of Energy (DOE) Office of Biological and Environmental Research. Oak Ridge National Laboratory is managed by UT-Battelle LLC for DOE under contract DE-AC05-00OR22725. Portions of this work were performed at the Stanford Synchrotron Radiation Lightsource (SSRL) and the Canadian Light Source (CLS). SSRL (a directorate of SLAC) is supported by the U.S. DOE, Office of Science, Office of Basic Energy Sciences under Contract No. DE-AC02-76SF00515. The CLS is supported by the Canadian Foundation for Innovation, Natural Sciences and Engineering Research Council of Canada, the University of Saskatchewan, the Government of Saskatchewan, Western Economic Diversification Canada, the National Research Council Canada, and the Canadian Institutes of Health Research. Logistical support while working on the Barrow Environmental Observatory (BEO) was provided by Umiaq, LLC.

References

Baldock JA, Skjemstad JO (2000) Role of the soil matrix and minerals in protecting natural organic materials against biological attack. Org Geochem 31(7):697–710

Bethke CM, Sanford RA, Kirk MF, Jin Q, Flynn TM (2011) The thermodynamic ladder in geomicrobiology. Am J Sci 311(3):183–210

Bockheim JG, Everett LR, Hinkel KM, Nelson FE, Brown J (1999) Soil organic carbon storage and distribution in arctic tundra, Barrow, Alaska. Soil Sci Soc Am J 63(4):934–940

Bockheim JG, Hinkel KM, Nelson FE (2003) Predicting carbon storage in tundra soils of arctic Alaska. Soil Sci Soc Am J 67(3): 948–950

Bond DR, Lovley DR (2002) Reduction of Fe(III) oxide by methanogens in the presence and absence of extracellular quinones. Environ Microbiol 4(2):115–124

Brown J (1969) Ionic concentration gradients in permafrost, Barrow, Alaska. Cold Regions Research and Engineering Lab, Hanover NH. No. CRREL-RR-272

Byrne JM, Klueglein N, Pearce C, Rosso KM, Appel E, Kappler A (2015) Redox cycling of Fe(II) and Fe(III) in magnetite by Fe-metabolizing bacteria. Science 347(6229):1473–1476

Chen J, Gu B, LeBoeuf EJ, Pan H, Dai S (2002) Spectroscopic characterization of the structural and functional properties of natural organic matter fractions. Chemosphere 48(1):59–68

Gu B, Schmitt J, Chen Z, Liang L, McCarthy JF (1994) Adsorption and desorption of natural organic matter on iron oxide: mechanisms and models. Environ Sci Technol 28(1):38–46

Gu B, Schmitt J, Chen Z, Liang L, McCarthy JF (1995) Adsorption and desorption of different organic matter fractions on iron oxide. Geochim Cosmochim Acta 59(2):219–229

Gu B, Mehlhorn TL, Liang L, McCarthy JF (1996) Competitive adsorption, displacement, and transport of organic matter on iron oxide: I. Competitive adsorption. Geochim Cosmochim Acta 60(11):1943–1950

Hansel CM, Benner SG, Neiss J, Dohnalkova A, Kukkadapu RK, Fendorf S (2003) Secondary mineralization pathways induced by dissimilatory iron reduction of ferrihydrite under advective flow. Geochim Cosmochim Acta 67(16): 2977–2992

Heimann M, Reichstein M (2008) Terrestrial ecosystem carbon dynamics and climate feedbacks. Nature 451(7176): 289–292

Herndon EM, Mann BF, Roy Chowdhury T, Yang Z, Wullschleger SD, Graham D, Liang L, Gu B (2015a) Pathways of anaerobic organic matter decomposition in tundra soils from Barrow, Alaska. J Geophys Res Biogeosci. doi:10.1002/2015JG003147

Herndon EM, Yang Z, Graham DE, Wullschleger SD, Gu B, Liang L (2015b) Surface and active layer pore water chemistry from ice wedge polygons, Barrow, Alaska, 2013–2014. In: Next generation ecosystem experiments arctic data collection, Carbon Dioxide Information Analysis Center, Oak Ridge National Laboratory, Oak Ridge. http://dx.doi.org/10.5440/1226245

Hinkel KM, Paetzold F, Nelson FE, Bockheim JG (2001) Patterns of soil temperature and moisture in the active layer and upper permafrost at Barrow, Alaska: 1993–1999. Global Planet Change 29(3):293–309

Hinkel KM, Frohn RC, Nelson FE, Eisner WR, Beck RA (2005) Morphometric and spatial analysis of thaw lakes and drained thaw lake basins in the western Arctic Coastal Plain, Alaska. Permafr Periglac Process 16(4):327–341

Hubbard SS, Gangodagamage C, Dafflon B, Wainwright H, Peterson J, Gusmeroli A, Wullschleger SD (2013) Quantifying and relating land-surface and subsurface variability in permafrost environments using LiDAR and surface geophysical datasets. Hydrogeol J 21(1):149–169

Jensen HS, Kristensen P, Jeppesen E, Skytthe A (1992) Iron: phosphorus ratio in surface sediment as an indicator of phosphate release from aerobic sediments in shallow lakes. In: Sediment/water interactions. Springer, Netherlands, pp 731–743

Karlsson T, Persson P (2010) Coordination chemistry and hydrolysis of Fe(III) in a peat humic acid studied by X-ray absorption spectroscopy. Geochim Cosmochim Acta 74:30–40

Karlsson T, Persson P (2012) Complexes with aquatic organic matter suppress hydrolysis and precipitation of Fe(III). Chem Geol 322:19–27

Karlsson T, Persson P, Skyllberg U, Mörth CM, Giesler R (2008) Characterization of iron(III) in organic soils using extended X-ray absorption fine structure spectroscopy. Environ Sci Technol 42(15):5449–5454

Kato S, Hashimoto K, Watanabe K (2012) Methanogenesis facilitated by electric syntrophy via (semi) conductive iron-oxide minerals. Environ Microbiol 14(7):1646–1654

Kim Y (2015) Effect of thaw depth on fluxes of CO2 and CH4 in manipulated Arctic coastal tundra of Barrow, Alaska. Sci Total Environ 505:385–389

Kokelj SV, Burn CR (2003) Ground ice and soluble cations in near-surface permafrost, Inuvik, Northwest Territories, Canada. Permafr Periglac Process 14(3):275–289

Kokelj SV, Burn CR (2005) Geochemistry of the active layer and near-surface permafrost, Mackenzie delta region, Northwest Territories, Canada. Can J Earth Sci 42(1):37–48

Koven CD, Lawrence DM, Riley WJ (2015) Permafrost carbon—climate feedback is sensitive to deep soil carbon decomposability but not deep soil nitrogen dynamics. Proc Natl Acad Sci 112(12):3752–3757

Lacelle D, Juneau V, Pellerin A, Lauriol B, Clark ID (2008) Weathering regime and geochemical conditions in a polar desert environment, Haughton impact structure region, Devon Island, Canada. Can J Earth Sci 45(10):1139–1157

Lara MJ, McGuire AD, Euskirchen ES, Tweedie CE, Hinkel KM, Skurikhin AN, Genet H (2014) Polygonal tundra geomorphological change in response to warming alters future CO2 and CH4 flux on the Barrow Peninsula. Glob Change Biol. doi:10.1111/gcb.12757

Liang L, Morgan JJ (1990) Chemical aspects of iron oxide coagulation in water: laboratory studies and implication for natural systems. Aquat Sci 52:32–55

Liang L, McCarthy JF, Jolley LW, McNabb JA, Mehlhorn TL (1993) Iron dynamics-observations of transformation during injection of natural organic matter in a sandy aquifer. Geochim Cosmochim Acta 57:1987–1999

Liang L, Hofmann A, Gu B (2000) Ligand-induced dissolution and release of ferrihydrite colloids. Geochim Cosmochim Acta 64(12):2027–2037

Liljedahl AK, Hinzman LD, Schulla J (2012) Ice-wedge polygon type controls low-gradient watershed-scale hydrology. In: Tenth International Conference on Permafrost, Salekhard

Lipson DA, Jha M, Raab TK, Oechel WC (2010) Reduction of iron (III) and humic substances plays a major role in anaerobic respiration in an Arctic peat soil. J Geophys Res. doi:10.1029/2009JG001147

Lipson DA, Zona D, Raab TK, Bozzolo F, Mauritz M, Oechel WC (2012) Water table height and microtopography control Biogeochemical cycling in an Arctic coastal tundra Ecosystem. Biogeosciences 9:577–591

Lipson DA, Raab TK, Goria D, Zlamal J (2013) The contribution of Fe(III) and humic acid reduction to ecosystem respiration in drained thaw lake basins of the Arctic Coastal Plain. Glob Biogeochem Cycles 27(2):399–409

Lovley DR, Phillips EJ (1988) Novel mode of microbial energy metabolism: organic carbon oxidation coupled to dissimilatory reduction of iron or manganese. Appl Environ Microbiol 54(6):1472–1480

Lovley DR, Stolz JF, Nord GL, Phillips EJ (1987) Anaerobic production of magnetite by a dissimilatory iron-reducing microorganism. Nature 330(6145):252–254

Brown J, Everett KR, Webber PJ, MacLean Jr, SF, Murray DF (1980) The coastal tundra at Barrow. An arctic ecosystem: the coastal tundra at Barrow, Alaska. pp 1–29

Metje M, Frenzel P (2007) Methanogenesis and methanogenic pathways in a peat from subarctic permafrost. Environ Microbiol 9(4):954–964

Miller KE, Lai CT, Friedman ES, Angenent LT, Lipson DA (2015) Methane suppression by iron and humic acids in soils of the Arctic Coastal Plain. Soil Biol Biochem 83:176–183

Moosavi SC, Crill PM (1998) CH4 oxidation by tundra wetlands as measured by a selective inhibitor technique. J Geophys Res 103(D22):29093–29106

Newman BD, Throckmorton HM, Graham DE, Gu B, Hubbard SS, Liang L, Wullschleger SD (2015) Microtopographic and depth controls on active layer chemistry in arctic polygonal ground. Geophys Res Lett 42(6):1808–1817

Paytan A, Lecher AL, Dimova N, Sparrow KJ, Kodovska FGT, Murray J, Kessler JD (2015) Methane transport from the active layer to lakes in the Arctic using Toolik Lake, Alaska, as a case study. Proc Natl Acad Sci 112(12):3636–3640

Pearce DME, Clymo RS (2001) Methane oxidation in a peatland core. Glob Biogeochem Cycles 15(3):709–720

Regier T, Krochak J, Sanders DA, Hu Y-F, Thompson J, Blyth RIR (2007) Performance and capabilities of the Canadian dragon: the SGM beamline at the Canadian light source, nuclear instruments and methods. Phys Res A 582: 93–95. Beamlines: SGM (11ID-1)

Regier T, Paulsen J, Wright G, Coulthard I, Tan K, Sanders DA, Blyth RIR (2007) Commissioning of the spherical grating monochromator (SGM) soft x-ray spectroscopy Beamline at the Canadian light source, Synchrotron Radiation Instrumentation: Ninth International Conference CP879, pp 473–476. Beamlines: SGM (11ID-1)

Rentz JA, Turner IP, Ullman JL (2009) Removal of phosphorus from solution using biogenic iron oxides. Water Res 43(7):2029–2035

Riley WJ, Subin ZM, Lawrence DM, Swenson SC, Torn MS, Meng L, Hess P (2011) Barriers to predicting changes in global terrestrial methane fluxes: analyses using CLM4Me, a methane biogeochemistry model integrated in CESM. Biogeosciences 8(7):1925–1953

Roden EE, Wetzel RG (1996) Organic carbon oxidation and suppression of methane production by microbial Fe(III) oxide reduction in vegetated and unvegetated freshwater wetland sediments. Limnol Oceanogr 41(8):1733–1748

Roy Chowdhury T, Herndon EM, Phelps TJ, Elias DA, Gu B, Liang L, Wullschleger SD, Graham DE (2015) Stoichiometry and temperature sensitivity of methanogenesis and CO_2 production from saturated polygonal tundra in Barrow, Alaska. Glob Change Biol 21(2):722–737

Schuur EA, Bockheim J, Canadell JG, Euskirchen E, Field CB, Goryachkin SV, Zimov SA (2008) Vulnerability of permafrost carbon to climate change: implications for the global carbon cycle. Bioscience 58(8):701–714

Schuur EA, Vogel JG, Crummer KG, Lee H, Sickman JO, Osterkamp TE (2009) The effect of permafrost thaw on old carbon release and net carbon exchange from tundra. Nature 459(7246):556–559

Shannon RD, White JR (1994) A three-year study of controls on methane emissions from two Michigan peatlands. Biogeochemistry 27(1):35–60

Shiklomanov NI, Streletskiy DA, Nelson FE, Hollister RD, Romanovsky VE, Tweedie CE, Bockheim JG, Brown J (2010) Decadal variations of active-layer thickness in moisture-controlled landscapes, Barrow, Alaska. J Geophys Res. doi:10.1029/2009JG001248

Smith LC, Sheng Y, MacDonald GM, Hinzman LD (2005) Disappearing arctic lakes. Science 308(5727):1429

Solomon D, Lehmann J, Kinyangi J, Liang B, Schäfer T (2005) Carbon K-edge NEXAFS and FTIR-ATR spectroscopic investigation of organic carbon speciation in soils. Soil Sci Soc Am J 69(1):107–119

Stocker TF, Qin D, Plattner GK, Tignor M, Allen SK, Boschung J, Midgley BM (2013) IPCC, 2013: climate change 2013: the physical science basis. Contribution of working group I to the fifth assessment report of the intergovernmental panel on climate change

Stolpe B, Guo L, Shiller AM, Aiken GR (2013) Abundance, size distributions and trace-element binding of organic and iron-rich nanocolloids in Alaskan rivers, as revealed by field-flow fractionation and ICP-MS. Geochim Cosmochim Acta 105:221–239

Sturtevant CS, Oechel WC (2013) Spatial variation in landscape-level CO2 and CH4 fluxes from arctic coastal tundra: influence from vegetation, wetness, and the thaw lake cycle. Glob Change Biol 19(9):2853–2866

Tarnocai C, Canadell JG, Schuur EAG, Kuhry P, Mazhitova G, Zimov S (2009) Soil organic carbon pools in the northern circumpolar permafrost region. Glob Biogeochem Cycles. doi:10.1029/2008GB003327

Throckmorton HM, Heikoop JM, Newman BD, Altmann GL, Conrad MS, Muss JD, Perkins GB, Smith LJ, Torn MS, Wullschleger SD, Wilson CJ (2015) Pathways and transformations of dissolved methane and dissolved inorganic carbon in Arctic tundra watersheds: evidence from analysis of stable isotopes. Global Biogeochem Cycles. doi:10.1002/2014GB005044

Turetsky MR, Treat CC, Waldrop MP, Waddington JM, Harden JW, McGuire AD (2008) Short-term response of methane fluxes and methanogen activity to water table and soil warming manipulations in an Alaskan peatland. J Geophys Res 113(G3):134

Ueyama M, Iwata H, Harazono Y, Euskirchen ES, Oechel WC, Zona D (2013) Growing season and spatial variations of carbon fluxes of Arctic and boreal ecosystems in Alaska (USA). Ecol Appl 23(8):1798–1816

von Fischer JC, Rhew RC, Ames GM, Fosdick BK, von Fischer PE (2010) Vegetation height and other controls of spatial variability in methane emissions from the Arctic coastal tundra at Barrow, Alaska. J Geophys Res 115(G4):33

Wainwright HM, Dafflon B, Smith LJ, Hahn MS, Curtis JB, Wu Y, Hubbard SS (2015) Identifying multiscale zonation and assessing the relative importance of polygon geomorphology on carbon fluxes in an Arctic Tundra Ecosystem. J Geophys Res. doi: 10.1002/2014JG002799

Webb SM (2005) SIXpack: a graphical user interface for XAS analysis using IFEFFIT. Phys Scr T115:1011–1014. doi:10.1238/Physica.Topical.115a01011

Weber KA, Achenbach LA, Coates JD (2006) Microorganisms pumping iron: anaerobic microbial iron oxidation and reduction. Nat Rev Microbiol 4(10):752–764

Weishaar JL, Aiken GR, Bergamaschi BA, Fram MS, Fujii R, Mopper K (2003) Evaluation of specific ultraviolet absorbance as an indicator of the chemical composition and reactivity of dissolved organic carbon. Environ Sci Technol 37(20):4702–4708

Wieder WR, Cleveland CC, Smith WK, Todd-Brown K (2015) Future productivity and carbon storage limited by terrestrial nutrient availability. Nat Geosci 8(6):441–444

Zhuang Q, Melillo JM, McGuire AD, Kicklighter DW, Prinn RG, Steudler PA, Hu S (2007) Net emissions of CH4 and CO2 in Alaska: implications for the region's greenhouse gas budget. Ecol Appl 17(1):203–212

Zona D, Lipson DA, Zulueta RC, Oberbauer SF, Oechel WC (2011) Microtopographic controls on ecosystem functioning in the Arctic Coastal Plain. J Geophys Res. doi:10.1029/2009JG001241

Zona D, Lipson DA, Paw U, Kyaw T, Oberbauer SF, Olivas P, Gioli B, Oechel WC (2012) Increased CO_2 loss from vegetated drained lake tundra ecosystems due to flooding. Glob Biogeochem Cycles. doi:10.1029/2011GB004037